

Theoretical Study of the Structural, Energetic, and Electronic Properties of 55-Atom Metal Nanoclusters: A DFT Investigation within van der Waals Corrections, Spin–Orbit Coupling, and PBE+U of 42 Metal Systems

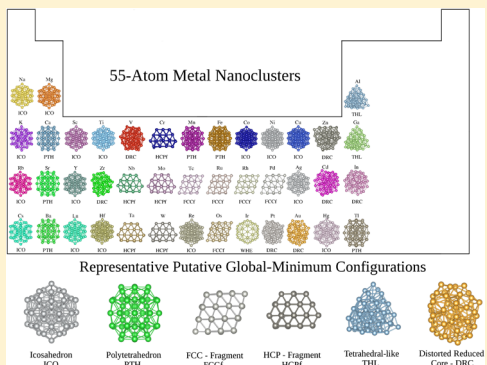
Maurício J. Piotrowski,[†] Crina G. Ungureanu,[‡] Polina Tereshchuk,[‡] Krys E. A. Batista,[†] Anderson S. Chaves,[‡] Diego Guedes-Sobrinho,[‡] and Juarez L. F. Da Silva^{*‡}

[†]Department of Physics, Federal University of Pelotas, P.O. Box 354, 96010-900 Pelotas, Rio Grande do Sul, Brazil

[‡]São Carlos Institute of Chemistry, University of São Paulo, P.O. Box 780, 13560-970 São Carlos, São Paulo, Brazil

S Supporting Information

ABSTRACT: An atom-level ab initio understanding of the structural, energetic, and electronic properties of nanoclusters with diameter size from 1 to 2 nm figures as a prerequisite to foster their potential technological applications. However, because of several challenges such as the identification of ground-state structures by experimental and theoretical techniques, our understanding is still far from satisfactory, and further studies are required. We report a systematic ab initio investigation of the 55-atom metal nanoclusters, (M_{55}), including alkaline, transitional, and post-transitional metals, that is, a total of 42 systems. Our calculations are based on all-electron density functional theory within the Perdew–Burke–Ernzerhof (PBE) functional combined with van der Waals (vdW) correction, spin–orbit coupling (SOC) for the valence states. Furthermore, we also investigated the role of the localization of the d states by using the PBE+U functional. We found a strong preference for the putative PBE global-minimum configurations for the compact Mackay icosahedron structure, namely, 16 systems (Na, Mg, K, Sc, Ti, Co, Ni, Cu, Rb, Y, Ag, Cs, Lu, Hf, Re, Hg), while several systems adopt alternative compact structures such as 6 polytetrahedron (Ca, Mn, Fe, Sr, Ba, Tl) and 10 structures derived from crystalline face-centered cubic and hexagonal close-packed (HCP) fragments (Cr, Nb, Mo, Tc, Ru, Rh, Pd, Ta, W, Os). However, the 10 remaining systems adopt less compact structures based on the distorted reduced-core structure (V, Zn, Zr, Cd, In, Pt, Au), tetrahedral-like (Al, Ga), and one HCP wheel-type (Ir) structure. The binding energy shows a quasi-parabolic behavior as a function of the atomic number, and hence the occupation of the bonding and antibonding states defines the main trends (binding energy, equilibrium bond lengths, etc.). On average, the binding energy of the M_{55} systems represents 79% of the cohesive energy of the respective bulk systems. The addition of the vdW correction changes the putative global-minimum configurations (pGMCs) for selected cases, in particular, for post-transitional metal systems. As expected, the PBE+U functional increases the total magnetic moment, which can be explained by the increased localization of the d states, which also contributed to increase the number of atoms in the core region (increase coordination) of the pGMCs. In contrast with the effects induced by the vdW correction and localization of the d states, the addition of the SOC coupling cannot change the lowest energy configurations, but it affects the electronic properties, as expected from previous calculations for 13-atom clusters.



I. INTRODUCTION

Metal particles with diameter from 1 to 10 nm (nanoclusters) have been widely studied as potential candidates for a wide range of technological applications, which includes nanocatalysis,^{1,2} selective release of drugs,^{3,4} antimicrobial agents,^{5,6} energy storage devices,^{7,8} and so on. At lower size regime, for example, from 1 to 2 nm diameter, every metal atom plays an important role in the structural, energetic, electronic, and thermodynamic properties,^{9–11} and hence, it provides the path to tune the chemical and physical properties of nanoclusters as a function of particle size,^{12,13} shape,¹³ charge state,¹⁴ chemical composition,^{12,15,16} and so on. Although metal particles with

different number of atoms can be obtained by physical or chemical techniques,^{9,11} their relative thermodynamic stability is system- and size-dependent; that is, particles with a particular number of atoms have higher energetic stability than others, which manifest themselves in mass spectra of gas-phase particles with high rate of occurrence. Thus those particles have been known as magic size particles.^{17–20}

Received: October 14, 2016

Revised: November 29, 2016

Published: November 29, 2016

Among a large number of magic size metal particles, 55-atom particles have attracted special interest^{9–11,15,16,19,21–30} due to their relatively higher energy stability for several metal systems, which can be explained by the formation of the closed-shell Mackay 55-atom icosahedron structures with I_h symmetry.³¹ The icosahedron structure with 55 atoms is composed of a center atom surrounded by two shells, namely, a first shell with 12 atoms and a second shell including the remaining 42 atoms. The 55 atoms are separated into five nonequivalent atoms, namely, one atom in the center, a second atom in the first shell, which represents the 12-atom, and three nonequivalent atoms represent the 42-atom surface,²⁶ which are separated in groups of 24, 12, and 6 atoms. Thus the core is composed of 13 atoms, while 76% of the atoms are located in the surface and exposed to the vacuum region. Furthermore, the icosahedron structure can be obtained by a transformation on the cuboctahedron (CUB) structure, which is a fragment of the face-centered cubic (FCC) structure.^{31–33}

In contrast with natural expectations based on the close-packed structures for metal systems,^{34,35} for example, FCC, it has been known that the icosahedron or CUB structures cannot yield the putative global-minimum configuration (pGMC) for a few metal systems,^{19,30} for example, Ag_{55} ,^{19,25,30} Pt_{55} ,^{19,26,30} and Au_{55} .^{19,21,26,29,30} Furthermore, because of the lack of systematic studies, our knowledge of the metal systems that do not adopt the icosahedron structure is incomplete. Thus although several studies have been reported so far, we will show below that our atomistic understanding of 55-atom nanoclusters is far from complete, in particular, due to several challenges, which include the search of the pGMC for M_{55} nanoclusters.

Photoelectron spectrometry has obtained strong evidence of an icosahedron-like structure for cationic alkali clusters, for example, Na_{55}^+ ,²² which was also supported by first-principles calculations for both cationic and neutral 55-atom nanoclusters.^{23,24} Thus it is a direct example where the geometric packing for alkali cluster is correlated with its electronic structure, as described by the Jellium model. Recently, a density functional theory (DFT) study reported a magnetic feature for the Na_{55} ²⁸ and K_{55} nanoclusters,³⁶ which was suggested as a preponderant property in the enhancement of the thermal stability of icosahedral Na_{55}^+ nanoclusters.³⁷ On the other side, for Cs_{55} , the geometric packing plays a dominant role in the stability of the icosahedron structure, which is explained by atomic characteristics, such as smaller size of the Cs atoms, relativistic effects, and sd hybridization.^{38–40}

Ab initio molecular dynamics indicated the important role of the geometric package for Cs_{55} based mainly on the surface stability of icosahedron-like structures, which largely contributes to the thermal stability.⁴¹ Rb_{55} is another important system of the alkali metal family, especially due to its applications as a partial component in systems for catalysis⁴² and biochemistry.⁴³ Guo et al.⁴⁴ analyzed the stability of the icosahedral configuration for Rb_{55} using DFT and X-ray photoelectron spectroscopy measurements, in which they observed a correlation between the presence of under-coordinated atoms and particular electronic properties, such as high electronic polarizability and electron density.

Among the alkaline-earth metals, Ca_{55} and Sr_{55} have been known as soft alkaline-earth metals once the structural features are strongly affected by pressure.^{45,46} Thus one of the principal features in alkaline-earth metals is the long-range interatomic forces when compared with d transition metals, and hence there is a complex relationship between size and stability.^{45,47}

For example, a pioneer study using mass spectroscopy showed that Sr nanoclusters with a few hundreds of atoms present structures in which the atoms are packaged in subshells.⁴⁸ This study was complemented by Wang et al.⁴⁹ using classical many-body potential with genetic algorithm (GA) and basin-hopping Monte Carlo (BHMC), which obtained the potential energy surface mapping for Sr_{55} and found the Mackay icosahedron structure as the putative global minimum configuration. However, this study showed that Sr clusters with 34 and 61 atoms are widely abundant, which is also observed for Ca including the sizes Ca_{37} , Ca_{39} , Ca_{45} , Ca_{53} , and Ca_{57} .^{46,48}

Additionally, even for Ca_{55} , the icosahedron configuration has been identified as the pGMC.⁴⁶ For Mg_{55} , Martin et al.⁴⁸ found the preference for icosahedral structures from the numbers of the Mackay's configurations through mass spectrometry, that is, Mg_{55} , Mg_{147} , Mg_{309} , and so on. An investigation by DFT indicated a correspondence between the band gap energy and the closed electronic shell for Mg_{55} , consequently contributing to the stability of the spherical symmetry of the structure.^{50–52} Using mass spectrometry, Ba_n clusters were determined with relative stability in a range of magic numbers between 13 and 32 atoms. On the other side, for larger sizes, such as Ba_{55} , the stability is not conclusive.⁵³ From that, many theoretical approaches have adopted the icosahedron structure for Ba_{13} ,^{54–56} while for Ba_{55} and larger ones this remain a challenge.

Using the technique of trapped ion electron diffraction (TIED) combined with DFT calculations,²⁵ Rapps et al.³⁰ systematically investigated 16 M_{55} nanoclusters, specifically Sc_{55} to Cu_{55} and Zr_{55} to Ag_{55} (except Y_{55} and Tc_{55}). Basically, they obtained four different structural motifs for the M_{55} systems, namely, icosahedron, polytetrahedral, irregular icosahedron, and close-packed fragments based on the FCC and hexagonal close-packed (HCP) crystalline structures. Moreover, Wang and Palmer²⁹ have used the aberration-corrected scanning transmission electron microscopy (STEM) to investigate Au_{55} . They found nonsymmetric structures, in agreement with previous ab initio studies,^{21,26} which reported low-symmetry (disordered) atomic structures in contrast with high-symmetry structures such as the icosahedron.

Furthermore, Li et al.,¹⁹ using ab initio DFT calculations, found that several TM_{55} nanoclusters are formed by FCC or HCP crystalline fragments, which was explained by the significant contribution of the edge atoms, that is, TM_{55} with short edge lengths and enlarged surface areas are energetically favorable. They point out that the classic Wulff construction principle should be generalized, including the edge atom contribution in the global energy minimization; consequently, they showed that all of the 55-atom 3d, 4d, and 5d TM nanoclusters prefer FCC or HCP crystal fragments on the contrary to the widely assumed icosahedron cluster, except the earliest and the latest elements in the periodic table. In the same context, Batista et al.⁵⁷ obtained a set of pGMC for Y_{55} , Zr_{55} , Nb_{55} , Mo_{55} , Tc_{55} , and Pt_{55} , on which they showed that the distorted reduced core (DRC) configuration is obtained for Zr_{55} , the same structural motif for Zn_{55} , Cd_{55} , Pt_{55} , and Au_{55} , and hence, they concluded that the preference for the DRC_{55} structure is related not only to the occupation of the antibonding d states but also to a combination of structural and electronic effects, namely, the valence electrons character and the atomic radius differences between internal and external nanocluster atoms.

Thus all previous studies provided a great contribution to improve our atomistic understanding of the mechanisms that drive the stability of 55-atom metal nanoclusters; however, there are only a few systematic studies that address the general problem of the identification of the pGMC to study the structural, energetics, electronic, and magnetic properties. Beyond that, from our knowledge, most of the theoretical investigations are based on plain DFT within semilocal functional, and hence, the effects of van der Waals corrections, spin-orbital coupling for the valence states, and the effects of the magnitude of the localization of the d states are unclear.

Therefore, to contribute to the understanding of the physical and chemical properties of 55-atom metals, we performed a systematic investigation of the pGMCs for 42 elements, which include alkali, alkali-earth, transitional (3d, 4d, and 5d), and post-transitional 55-atom metal systems. Furthermore, to address the role of the different approximations employed in this study, we considered van der Waals corrections, which might provide an important contribution to particular nanoclusters, spin-orbit coupling (SOC) for the valence electrons for selected systems. Lastly, we investigate the role of the magnitude of the localization of the d states, which can also affect the results, in particular, magnetic moments.

II. THEORETICAL APPROACH AND COMPUTATIONAL DETAILS

II.A. Total Energy Calculation. Our total energy calculations are based on spin-polarized DFT^{58,59} within the semilocal⁶⁰ Perdew–Burke–Ernzerhof⁶¹ (PBE) formulation to the exchange-correlation (XC) energy functional, as implemented in the Vienna ab initio simulation package (VASP, version 5.3.5).^{62,63} Recently, DFT+U calculations for TM₁₃ clusters⁶⁴ showed that the magnitude of the on-site Coulomb, U , and exchange, J , interactions⁶⁵ can affect the relative stability of the Co₁₃ and Rh₁₃ configurations due to the changes in the localization of the d states, which can modify the hybridization of the electronic sp-d states. For example, they found that an increased localization of the d states favors compact structures such as the icosahedron structure³¹ instead of open structures such as the double-simple-cubic (DSC) structure.⁶⁶ However, this effect is system-dependent,⁶⁴ and it is unclear whether it plays a crucial role for larger particles such as M_{55} .

Thus to improve our atomistic understanding of the d-state localization effects on the atomic structure of finite size systems, we employed the rotationally invariant approach proposed by Dudarev et al.,⁶⁷ in which only the difference between the U and J parameters is taken into account, that is, $U_{\text{eff}} = U - J$. Our goal is to address the effects of the d state localization on the most important physical and chemical properties, and hence we selected a particular set of systems, namely, Fe₅₅, Co₅₅, Ni₅₅, Ru₅₅, Rh₅₅, and Pd₅₅, and a U_{eff} parameter of 2.0 eV for the d states, which is large enough to affect the localization of the d states,⁶⁴ and compared the results with DFT-PBE.

It has been known that local or semilocal XC functional^{60,61} cannot provide a correct description of the nonlocal long-range vdW interaction,⁶⁸ which is crucial to improve the description of the magnitude of the binding energy for weak binding systems.^{68–82} Thus several vdW energy corrections based on pairwise additive interactions have been proposed, namely, the Tkatchenko–Scheffler (TS) correction without and with self-consistent screening (SCS) effects^{75,78} and the D2 and D3 corrections proposed by Grimme.^{71,76} To improve the description of the vdW interaction in M_{55} , we employed the

TS+SCS vdW correction⁷⁸ as implemented by Bučko et al.⁸⁰ in VASP^{62,63} and discussed in detail elsewhere.^{80,83} To investigate the role of the vdW correction for M_{55} , we selected only the Al₅₅, Cu₅₅, Zn₅₅, Ga₅₅, Ag₅₅, Cd₅₅, In₅₅, Au₅₅, Hg₅₅, and Tl₅₅ systems, in which the vdW correction might play a crucial role.

For all DFT calculations, the electrons are described by the scalar-relativistic approximation,^{84,85} in which the SOC is taken into account for the core states but neglected for the valence states; however, previous results found that SOC plays a crucial role for heavy elements systems.^{66,86,87} For example, the putative global minimum configuration (pGMC) of Au₁₃ changes from planar to 3D structures upon the addition of the SOC for the Au valence states; however, it is important to mention that the magnitude of the energy difference is \sim 10 meV/atom.⁶⁶ Thus in this work DFT-PBE calculations with and without SOC for the valence states were performed for the Os₅₅, Ir₅₅, Pt₅₅, Au₅₅, Hg₅₅, and Tl₅₅ systems. For those calculations, the number of bands was increased to twice the number of electrons in the system to achieve good convergence.

The Kohn–Sham equations were solved using the all-electron projected augmented wave (PAW) method,^{88,89} as implemented in VASP (version 5.3.5),^{62,63,90} where the Kohn–Sham states are described by plane-waves. For all total energy calculations, we employed the PAW projectors provided within VASP and the respective recommended cutoff energy, which are summarized in the Supporting Information. For the bulk systems, the equilibrium volumes were obtained by optimization of the stress tensor and atomic forces using a cutoff energy two times larger than the recommended cutoff energy in the PAW projectors, which is required due to the slow convergence of the stress tensor as a function of the number of plane-waves. All cutoff energies are reported in the Supporting Information.

To minimize the interactions among the M_{55} nanocluster and their periodic images, we employed cubic boxes with a minimum distance of 12 Å between the nanocluster surfaces for all calculations. Thus, due to the differences in the atomic radius of every species,^{34,35,91} which defines the M_{55} nanocluster size, we employed cubic boxes with different lattice size, for example, from 22 to 33 Å. All values are reported in the Supporting Information. For the Brillouin zone (BZ) integration, we employed a single k-point (Γ -point) for the nanoclusters and free-atom calculations once there is no dispersion in the electronic states within the BZ, while a k-point density of 50 Å⁻³ was used for all bulk calculations, which yields a k-mesh of 22 × 22 × 22 for Pt in the FCC structure. For all total energy optimizations, the equilibrium geometry was obtained once the atomic forces on every atom were <0.025 eV/Å with a total energy convergence of 1.0×10^{-5} eV. For the PBE+vdW calculations, we increase the total energy convergence to 1.0×10^{-7} eV to obtain well-converged electron densities, which is required by the TS-SCS vdW correction;^{75,78} however, our convergence tests indicated that 1.0×10^{-5} eV can yield similar relative total energies. The convergence parameters were tested, and further details are reported in the Supporting Information.

II.B. Atomic Structure Configurations. The search of the pGMC for M_{55} nanoclusters is a challenging problem as experimental techniques such as X-ray diffraction cannot directly access the atomic structure (x, y, z positions) due to the lack of long-range order,^{92–94} which is present in bulk materials.^{34,35} Recently, STEM combined with theoretical modeling has been employed to refine structural models for

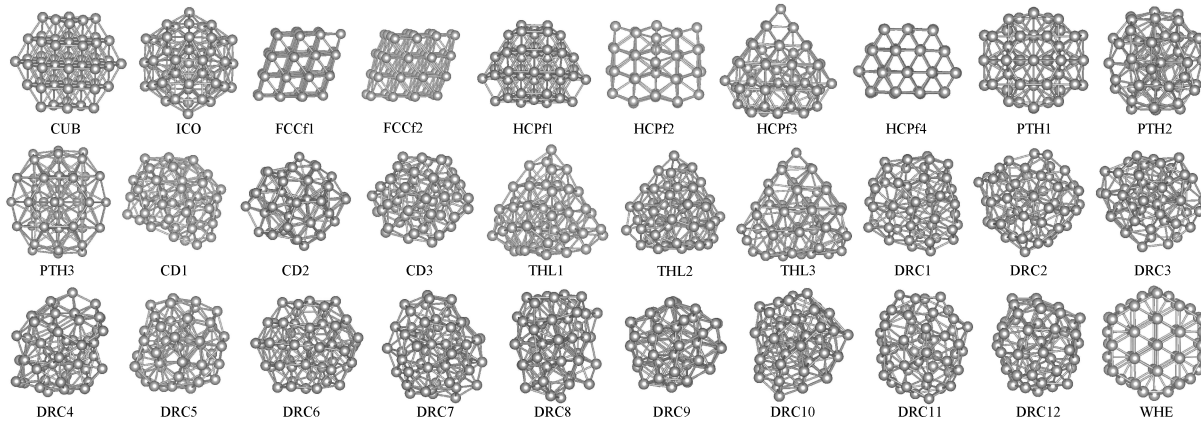


Figure 1. Most important trial configurations selected for total energy calculations for the M_{55} nanoclusters. The structural name is indicated below every configuration, namely, cuboctahedron (CUB), icosahedron (ICO), face-centered cubic fragment (FCCf), hexagonal close-packed fragment (HCPf), polytetrahedron (PTH), chiral distorted (CD), tetrahedral-like (THL), disordered reduced-core (DRC), and hexagonal close-packed wheel-type (WHE) structures. The atomic positions are reported in the [Supporting Information](#) along with further configurations.

large gold nanoparticles (~ 6000 atoms),⁹⁵ while Erickson et al.⁹⁶ obtained the first successful isolation and crystallographic characterization of Pd-based 55-atom two-shell icosahedral particles. Thus although progress has been made, a direct determination of the structure of nanoclusters is still a challenge.

Thus several global optimization algorithms have been employed to search the pGMC of finite size systems, namely, GA,^{97,98} BHMC,^{99,100} conformation space annealing (CSA),¹⁰¹ and so on. Along a global optimization for a finite-size particle, those algorithms can also identify a large number of higher energy local minimum configurations (LMCs), which can play an important role in obtaining a deep understanding of the potential energy surface.^{102,103} Furthermore, LMCs can help us to understand experimental results obtained at high temperatures; that is, it is unlikely that pGMC structures are preserved at high temperatures due to atomic structure distortions and phase transitions induced by temperature effects.

In most of the GA,^{97,98} BHMC,^{99,100} and CSA¹⁰¹ implementations, the interactions among the atoms are described by empirical pair-potentials (EPPs) such as Lennard-Jones¹⁰⁴ and Sutton-Chen,¹⁰⁵ which play a crucial role in reducing the computational cost to perform from 10^3 to 10^6 total energy evaluations along a global optimization. Furthermore, the embedded-atom method^{106,107} (EAM) has also been employed in the study of metallic and bimetallic particles,^{13,108,109} which includes a recent BHMC-EAM investigation of the structural and energetic properties of ZrCu, ZrAl, and CuAl nanoalloys with up to 561 atoms.¹³

Although those studies have provided a great contribution to improve our atomistic understanding of finite-size particles,^{13,100,110–112} EPP and EAM cannot provide an atomistic description at the same level as first-principles DFT calculations, which is essential to describe the fine details originated from quantum-size effects at finite-size particles; for example, the electronic levels are discrete and large magnetic moments can arise at finite-size particles.^{113,114} However, the combination of DFT calculations with global optimization algorithms, for example, GA or BHMC, has been restricted for small systems,^{100,115} which is not the case for the M_{55} particles.

To obtain the pGMC and high-energy LMC for the selected 55-atom metal nanoclusters, which can be used to understand the structural, energetic, and electronic properties as a function

of the atomic number and occupation of the valence states, we employed a set of about 25 to 40 structural candidates composed of a wide range of atomic environments for the 55-atom particles, which include high-symmetry compact and open structures, low-symmetry configurations, and bulk fragments (Figure 1), for example, the CUB structure with O_h symmetry, which is a fragment of the FCC crystal structure, the icosahedron (ICO) structure with I_h symmetry,³¹ the family of polytetrahedron (PTH) structures,¹¹⁶ tetrahedral-like (THL),²⁷ a family of the DRC structure, which includes distorted structures with 7 to 11 atoms in the core region,^{21,26,29} chiral distorted (CD),^{21,29} a set of fragments of the HCP structure (HCPf),³⁰ which includes the double-layer wheel (WHE) structure,¹⁹ and fragments of the FCC structure (FCCf).³⁰ The atomic positions of all trial configurations are reported in the [Supporting Information](#).

Furthermore, we performed crossover among the systems; that is, an identified pGMC for a particular system was used for several nearby systems in the periodic table. Initially, the geometric optimization for all systems was performed using DFT-PBE, while the PBE+U, PBE+vdW, and PBE+SOC calculations were performed for selected systems starting from all of the DFT-PBE optimized configurations.

III. RESULTS

We discuss the structural, energetic, electronic, and magnetic properties of the pGMC and high-energy LMC for all of the studied 42 metal nanoclusters.

III.A. Relative Total Energy. To quantify the spread of the energy among all calculated configurations, which depends on the nature of the chemical bonding between the atoms and selected configurations,⁶⁶ we calculated the relative total energy, ΔE_{tot} , for every atomic configuration, E_{tot}^i , with respect to the ICO structure with I_h symmetry, $E_{\text{tot}}^{\text{ICO}}$, that is, $\Delta E_{\text{tot}} = E_{\text{tot}}^i - E_{\text{tot}}^{\text{ICO}}$. In the ideal ICO₅₅ structure there are only five nonequivalent atoms, namely, center atom, first shell, and three nonequivalent atoms in the second shell exposed to the vacuum region.²⁶ The ΔE_{tot} results are shown in Figure 2, where the negative (positive) values indicate a configuration with lower (higher) energy than the ideal ICO structure.

We found that the magnitude of the relative energy difference between the pGMC and the highest-energy configurations is larger for TM₅₅ than for alkaline- and alkali-

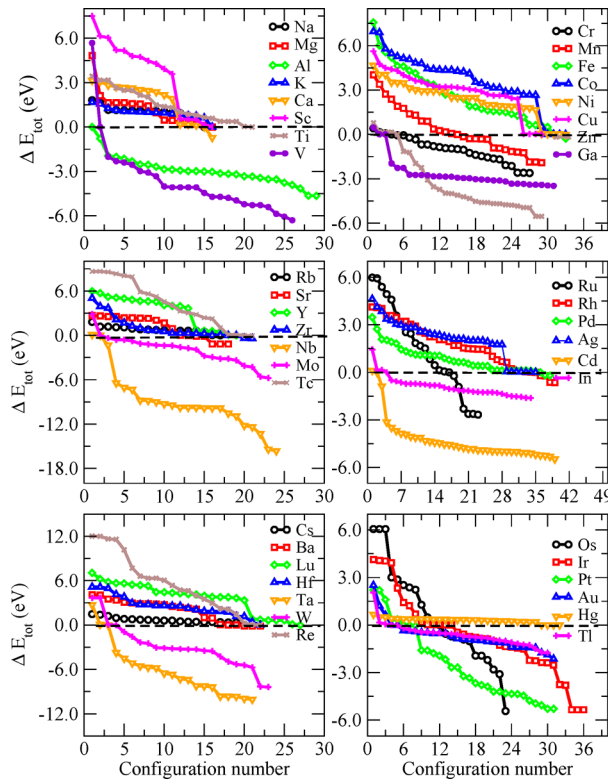


Figure 2. Relative total energies, ΔE_{tot} , for all calculated M_{55} configurations with respect to the ideal ICO structure with I_h symmetry, which is indicated by the dashed horizontal lines.

earth metals, in particular, for TM systems with nearly half-occupied d states, which is the case for V_{55} , Nb_{55} , and Ta_{55} . This trend can be explained as follows: (i) The correct magnetic local moment configurations of antiferromagnetic (AFM) or ferrimagnetic (FIM) solutions are important to obtain the energy gain, which affects the relative energy spread

among all configurations. Furthermore, the formation of directional bonds among the d states also plays an important role. (ii) Nanoclusters composed of atoms with nearly spherical valence orbitals, such as alkaline- and alkali-earth, cannot form directional bonds and hence the dependence on the relative energies is less sensitive to the structural details. For example, Hg_{55} is a special case due to the smaller magnitude of the energy spread among all calculated configurations, that is, 0.7 eV, which can be attributed to the spherical nature of the valence orbitals and weak interaction among the orbitals.

III.B. Putative Global Minimum Configurations. All of the DFT-PBE pGMCs for the 55-atom nanoclusters are shown in Figure 3, while their atomic coordinates are provided in the Supporting Information. We found a strong preference of the compact structures for pGMC, for example, 16 ICO, 6 PTH, 5 FCCf, and 5 HCPf, which is expected, as the metal crystalline structures are based on compact structures, for example, FCC, body-centered cubic (BCC), and HCP.^{34,35} The remaining pGMCs are based on less compact configurations such as the DRC (7), THL (2), and WHE (1) structures. The ideal ICO structure³¹ with I_h symmetry yields the pGMC for Na, Mg, K, Sc, Co, Ni, Cu, Rb, Y, Ag, Cs, Lu, and Hg, while a slightly distorted ICO structure was obtained for Ti, Hf, and Re, which are 0.37, 0.40, and 0.24 eV lower in energy than the ideal ICO structure.

Thus it indicates that free atoms with spherical electron densities might favor the formation of ICO_{55} structures. The ICO structure maximizes the sphericity of the particle, which is composed of an atom located at the center of gravity, a first shell with 12 equivalent atoms, and a second shell composed of 42 atoms separated in three groups of nonequivalent atoms, which forms interconnected compact (111)-like facets. Our results are consistent with the pGMC obtained by Rapps et al. for Sc, Co, Ni, Cu, and Ag employing combined experimental and theoretical techniques.³⁰ Furthermore, they reported an ICO structure as pGMC also for Pd, however, our pGMC for Pd is 0.21 eV lower in energy than ICO. Our ICO_{55}^{pGMC} results

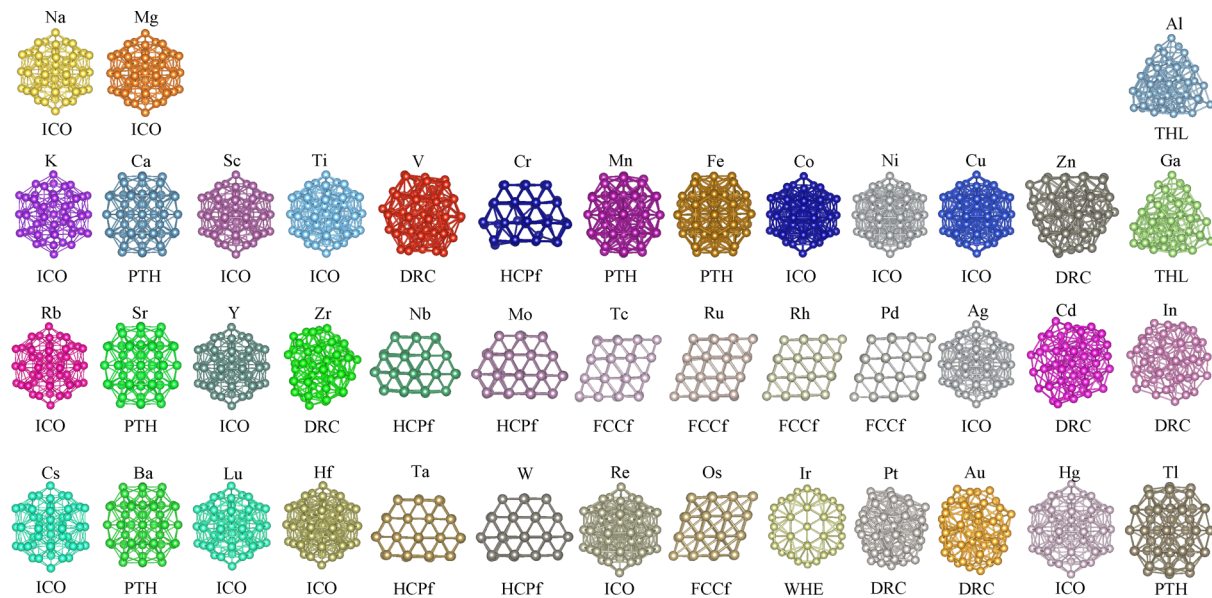


Figure 3. Putative global minimum configurations obtained by DFT-PBE calculations for the 55-atom metal nanoclusters. The chemical elements are indicated above every structure, while the structural name is indicated below every structure, namely, icosahedron (ICO), polytetrahedron (PTH), disordered reduced-core (DRC), hexagonal close-packed fragment (HCPf), face-centered cubic fragment (FCCf), tetrahedral-like (THL), and hexagonal close-packed wheel-type (WHE) structures. The atomic positions for all the pGMC are provided in the Supporting Information.

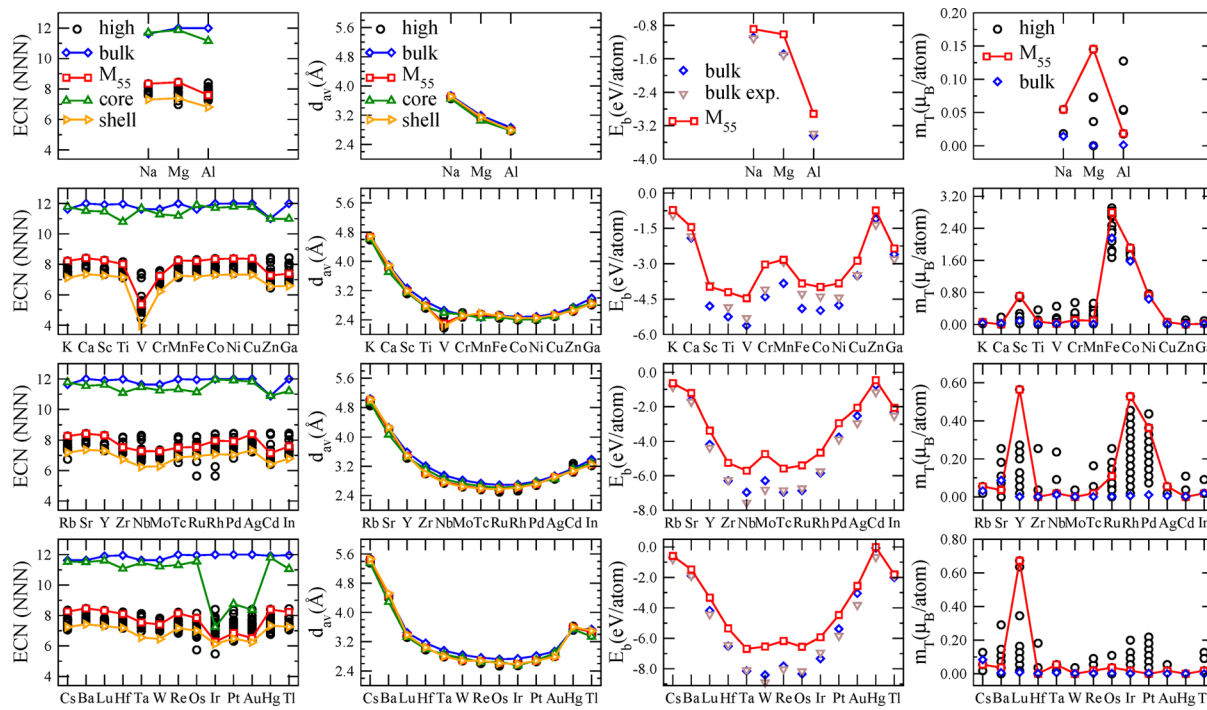


Figure 4. Effective coordination number (ECN) in number of nearest-neighbors (NNN), average weighted bond lengths, d_{av} (\AA), binding energy per atom, E_b (eV per atom), total magnetic moment per atom, m_T (μ_B per atom), for the putative global minimum configurations, M_{55} (\square), and high-energy local minimum configurations (\circ). Results for the respective systems in their respective lowest energy bulk structures are also shown for comparison (blue \diamond). The ECN and d_{av} were calculated for the core (\triangle) and surface (\triangleright) atoms.

for the 16 metals are also consistent with several theoretical results.^{15,16,52,57,110,117–119}

The PTH structure, which can be described by the combination of four interpenetrating 19-atoms double icosahedra,¹¹⁶ yields the pGMC for six systems, namely, Ca, Mn, Fe, Sr, Ba, and Tl. The PTH has a reduced sphericity compared with ICO; however, its average coordination number is higher than ICO due to the presence of high-coordinated atoms located in the core region; for example, the core atoms have coordination from 12 to about 15 instead of 12 observed in the ICO core. From the PTH family with C_{2v} symmetry, two PTH pGMC types are obtained; namely, (i) the $\text{PTH}_{55}^{\text{Fe}}$ structure has 12 atoms in the core region instead of 13 atoms as in the ICO structure and 43 atoms in surface region and (ii) for Ca, Sr, Ba, Mn, and Tl, we obtain a more compact PTH structure, which contains 14 atoms in the core and only 41 atoms in the surface. The basic difference between both PTH structures is obtained by a 90° rotation of one of the interpenetrating 19-atom double icosahedra, which affects the number of atoms in the core and surface. Our results are in agreement with the pGMC obtained by Rapps et al.³⁰ only for the Mn_{55} and Fe_{55} nanoclusters, while the pGMC for $\text{DRC}_{55}^{\text{Cr}}$, $\text{HCP}_{55}^{\text{Cr}}$, $\text{HCP}_{55}^{\text{Nb}}$, and $\text{HCP}_{55}^{\text{Mo}}$ is 3.22, 1.14, 5.87, and 4.99 eV lower in energy than the PTH configurations.

The FCCf and HCPf structures yield the pGMC for 10 TM systems, namely, 5 FCCf (Tc, Ru, Rh, Pd, Os) and 5 HCPf (Cr, Nb, Mo, Ta, W). Thus from these results we can conclude that the presence of partially occupied d states might favor the formation of defected (stacking faults) bulk-fragment structures instead of the CUB structure with O_h symmetry, which is also a fragment of the FCC structure; however, it does not contain structural defects such as in FCCf and HCPf. Beyond the energetically favorable facets, the FCCf and HCPf structures

have a reduced number of edge atoms, which decreases the corrugation of the surface.^{19,30} Furthermore, the CUB structure has a higher ratio of open (100) (higher surface energy) than compact (111) facets (lower surface energy), and hence it is not a pGMC. For Rh, Pd, and Os, the FCCf structure has 10 (45) atoms in the core (surface) region, while for Tc and Ru the FCC-fragment has only 8 atoms in the core region. For HCPf, we have also observed two types of structures: For Cr, Mo, and W, the HCPf structure has 10 (45) atoms in the core (shell) region, while for Nb and Ta the HCP fragment also has 10 core atoms, although it is based on a different HCP stacking fault, with shorter total edge lengths. Our results are in agreement with the pGMC reported by Rapps et al.³⁰ only for Ru and Rh.

The DRC structure yields the pGMC for seven systems, namely, V, Zn, Zr, Cd, In, Pt, and Au. DRC consists of a family of disordered nonsymmetric structures composed of a reduced core size;^{21,26,29} that is, there are from 7 to 11 atoms in the core region instead of 13 atoms as in the ICO structure, while the remaining atoms are located in the surface. Furthermore, those structures were also classified as CD structures.^{21,29} For Pt and Au, where there are 9 and 7 atoms in the core, respectively, the DRC structures are 5.64 and 2.14 eV lower in energy than ICO. Thus it indicates a large energy gain due to the changes in the structures; however, from our knowledge, there is no clear atomistic mechanism to explain these results. Our results for Pt and Au are consistent with previous DFT calculations;^{21,26,29} however, we would like to point out that DRC yields the pGMC for V and Zr, which is in disagreement with the results of Rapps et al.;³⁰ that is, they obtained an irregular icosahedral geometry with C_1 symmetry instead of the DRC structure.

The THL structure yields the pGMC for Al_{55} and Ga_{55} , while we obtained the WHE structure (pGMC) only for Ir_{55} . As

mentioned above, THL has only 10 atoms in the core region instead of 13 (ICO), where the core forms a tetrahedral pyramid and the surface is composed of four FCC (111) facets. WHE is also a reduced-core structure with seven atoms in the core region, consisting of a three-layered structure, similar to a “wheel” with a double defect. Our results are in agreement with the pGMC obtained by Kang et al.²⁷ for Al. The WHE pGMC follows the prediction given by Li et al.,¹⁹ where the surface is maximized and core region is reduced, keeping small edge length values.

III.C. Effective Coordination Number and Bond Lengths.

To improve the structural characterization of the 55-atom nanoclusters, we employed the effective coordination concept,^{120–122} which yields the effective coordination number (ECN_i) and the weighted bond lengths, d_{av}^i , for each atom *i* in the particle.⁶⁶ The average ECN and d_{av} results for the atoms located in the core and surface and for all of the 55 atoms are shown in Figure 4 as a function of the atomic number. Except for a few cases, the studied metals crystallize in one of the compact structures, namely, FCC, BCC, and HCP,^{34,35} where the ECN ranges from 11.6 NNN¹²² (BCC) to 12.0 NNN (FCC), while it depends on the c_0/a_0 ratio for the HCP structure; that is, it is 12.0 NNN for the ideal HCP structure ($c_0/a_0 = 1.633$). For example, there are small deviations in the values of ECN for particular HCP systems, for example, bulk Zn, which can be explained by the large value of the c_0/a_0 parameter (1.88) due to the weak interaction among the layers along the [0001] direction.

For the core atoms, which are not exposed to the vacuum region, the ECN is close to the values obtained for the bulk systems, which is expected due to the size of the core region (i.e., nearly 13 atoms in most of the configurations). However, there are clear exceptions, for example, Ir₅₅, Pt₅₅, and Au₅₅, which can be explained by the reduction of the core region (7, 9, and 7 atoms, respectively) compared with compact systems such as the ICO configuration with 13 atoms in the core. The surface atoms, which are exposed to the vacuum region, have an average ECN of ~7.0 NNN; however, it changes a lot for V₅₅, which reduces to nearly 4.0 NNN. Beyond that, there are small changes in the ECN of the surface atoms due to the differences in the surface of the nanoclusters, which relaxes to lower the total energy of the systems.

As expected, the average weighted bond lengths, d_{av} , for the bulk and nanoclusters follow almost exactly the same parabolic behavior as a function of the atomic number; that is, the differences are tiny. The lower coordination of the surface atoms or distortions in the nanoclusters does not affect the trends in the magnitude of the bond length. The largest bond lengths occur for the alkali metals, which can be explained by the largest atomic radius of the alkali systems and the weaker binding energy among the alkali atoms. The smallest bond lengths occur for systems with nearly half occupation of the d states. In 3d systems, for example, we can see small deviations in parabolic behavior, as in the case of Cr to Fe, which can be explained by the role played by the magnetic interactions, for example, AFM for bulk Mn and Cr and ferromagnetic (FM) for bulk Fe and Co. The trends in the average bond lengths will be explained below.

Considering the hard-sphere model,¹²³ the atomic radius estimated as $d_{av}/2$ can be correlated with the atomic coordination;⁵⁷ that is, the atomic radius is smaller (larger) for lower-coordinated (higher-coordinated) systems once the same number of electrons are shared by a smaller (larger)

number of bonds, and hence the bonds are stronger (weaker) and shorter (longer). From Figure 4, we observe two behaviors considering the d_{av} values for core and surface atoms: For pGMC based on highly coordinated structures, such as ICO and PTH, the d_{av} values for the core atoms are smaller than those for the surface atoms, while for pGMC with reduced core region, for example, DRC and bulk-fragments, the opposite behavior is observed. Both behaviors are in total agreement with the structural models as the core atoms are larger (smaller) than shell atoms for the DRC and bulk-fragments (ICO and PTH).

III.D. Binding Energy. To obtain further insights, we calculated the binding energy per atom, E_b , for the M_{55}^{pGMC} systems, which can be obtained using the following equation

$$E_b = E_{\text{tot}}^{\text{pGMC}} - E_{\text{tot}}^{\text{free-atom}} \quad (1)$$

where $E_{\text{tot}}^{\text{pGMC}}$ is the total energy per atom of the M_{55}^{pGMC} system, while $E_{\text{tot}}^{\text{free-atom}}$ is the total energy of the M free atom. Furthermore, for comparison, we also calculated the binding energy for their respective ground-state bulk structures, for example, FCC, BCC, HCP. For systems with complex structures, we considered the lowest energy configuration among the FCC, BCC, and HCP structures. The results are shown in Figure 4.

We obtained that the M_{55}^{pGMC} binding energy as a function of the atomic number has nearly the same behavior as the binding energy of the respective bulk systems, which is also the same as obtained from the experimental binding energy results.³⁴ Thus our results are also consistent with the results obtained for TM_{13}^{pGMC} ,⁶⁶ that is, the same trend is reproduced even for 13-atom clusters. At least for the 3d, 4d, and 5d TM systems, the behavior of the binding energy as a function of the atomic number can be explained by the occupation of the bonding and antibonding d states, which are located at lower and higher energies, respectively.¹²⁴ Thus the bonding d states are occupied first, and it increases the occupation from left to right along of the period, which contributes to increase the strength of the binding energy, and it reaches the maximum strength at ~50% occupation of the d states. Then, the occupation of the antibonding states starts, which contributes to decrease the magnitude of the binding energy, and it reaches the smallest value at the maximum occupation of the d states, that is, d^{10} . The deviation from a parabolic behavior for the 3d-states can be explained by the AFM interactions among the ions. Furthermore, due to the nature of the orbitals in the alkali metals (s states), their respective binding energies are even smaller, which is expected due to the small overlap of the s states and their delocalized character.

The size limit, in which the binding energy reaches the respective bulk value, is an important question in nanoscience, in particular, for TM particles. We found that the M_{55}^{pGMC} binding energies are, on average, 79% of the respective bulk values, in which the lower and higher limits are 67% (Zn₅₅) and 91% (Ga₅₅), respectively. Furthermore, it can be seen from Figure 4 that the difference is larger for the metal systems with the largest binding energies, while a 55-atom particle for the alkali metals nearly reproduces the bulk binding energy. The relative energy between the binding energies for the 55-atom and bulk is proportional to the surface energy, which is larger (smaller) for systems with larger (smaller) cohesive energy, and hence it explains the trends in Figure 4.

III.E. Total Magnetic Moments. The total magnetic moments per atom, m_T , for all M_{55} structures are shown in

Table 1. Relative Total Energies with Respect to the Ideal Icosahedron (ICO) Structure with I_h Symmetry, $\Delta E_{\text{tot}} = E_{\text{tot}}^i - E_{\text{tot}}^{\text{ICO}}$, Binding Energy Per Atom, E_b , total magnetic moment, m_T , Average Weighted Bond Lengths, d_{av} , and Effective Coordination Number, ECN, in Number of Nearest-Neighbors (NNN)^a

M_{55}	$\Delta E_{\text{tot}}^{\text{PBE}}$ (eV)	$\Delta E_{\text{tot}}^{\text{PBE+vdW}}$ (eV)	E_b^{PBE} (eV)	$E_b^{\text{PBE+vdW}}$ (eV)	m_T^{PBE} (μ_B)	$m_T^{\text{PBE+vdW}}$ (μ_B)	$d_{\text{av}}^{\text{PBE}}$ (Å)	$d_{\text{av}}^{\text{PBE+vdW}}$ (Å)	$\text{ECN}^{\text{PBE}b}$	$\text{ECN}^{\text{PBE+vdW}b}$
Al	-4.64 (THL)	-1.57 (THL)	-2.92	-3.08	1	1	2.79	2.77	7.60 (10)	7.58 (10)
Cu	0.00 (ICO)	0.00 (ICO)	-2.87	-3.12	3	3	2.52	2.49	8.38 (13)	8.40 (13)
Zn	-5.55 (DRC)	-4.41 (DRC)	-0.74	-0.86	0	0	2.66	2.65	7.27 (9)	7.27 (9)
Ga	-3.48 (THL)	-1.82 (DRC)	-2.35	-2.52	1	1	2.84	2.81	7.39 (10)	6.79 (10)
Ag	0.00 (ICO)	0.00 (ICO)	-2.06	-2.28	3	3	2.90	2.87	8.39 (13)	8.41 (13)
Cd	-5.48 (DRC)	-4.52 (DRC)	-0.46	-0.62	0	0	3.07	3.04	7.14 (9)	6.77 (9)
In	-1.62 (DRC)	-0.65 (PTH)	-2.07	-2.28	1	1	3.25	3.33	7.59 (10)	8.30 (14)
Au	-2.14 (DRC)	-1.15 (DRC)	-2.56	-2.69	1	1	2.80	2.79	6.52 (7)	6.49 (7)
Hg	0.00 (ICO)	-0.35 (PTH)	-0.01	-0.14	0	0	3.59	3.77	8.39 (13)	7.73 (14)
Tl	-1.75 (PTH)	-1.49 (PTH)	-1.81	-2.17	1	1	3.46	3.44	8.22 (14)	8.21 (14)
M_{55}	$\Delta E_{\text{tot}}^{\text{PBE}}$ (eV)	$\Delta E_{\text{tot}}^{\text{PBE+U}}$ (eV)	E_b^{PBE} (eV)	$E_b^{\text{PBE+U}}$ (eV)	m_T^{PBE} (μ_B)	$m_T^{\text{PBE+U}}$ (μ_B)	$d_{\text{av}}^{\text{PBE}}$ (Å)	$d_{\text{av}}^{\text{PBE+U}}$ (Å)	$\text{ECN}^{\text{PBE}b}$	$\text{ECN}^{\text{PBE+U}b}$
Fe	-0.29 (PTH)	-0.10 (PTH)	-3.84	-3.14	154	166	2.50	2.55	8.23 (12)	8.21 (14)
Co	0.00 (ICO)	0.00 (ICO)	-3.99	-3.22	105	105	2.44	2.47	8.36 (13)	8.29 (13)
Ni	0.00 (ICO)	0.00 (ICO)	-3.83	-4.16	40	50	2.44	2.45	8.38 (13)	8.39 (13)
Ru	-2.67 (FCCf)	-0.12 (FCCf)	-5.40	-3.94	6	12	2.58	2.61	7.55 (8)	7.88 (10)
Rh	-0.65 (FCCf)	-0.80 (FCCf)	-4.66	-3.35	29	53	2.63	2.61	7.96 (10)	7.96 (10)
Pd	-0.21 (FCCf)	-0.18 (FCCf)	-2.94	-2.44	20	26	2.72	2.70	7.92 (10)	7.93 (10)
M_{55}	$\Delta E_{\text{tot}}^{\text{PBE}}$ (eV)	$\Delta E_{\text{tot}}^{\text{PBE+SOC}}$ (eV)	E_b^{PBE} (eV)	$E_b^{\text{PBE+SOC}}$ (eV)	m_T^{PBE} (μ_B)	$m_T^{\text{PBE+SOC}}$ (μ_B)	$d_{\text{av}}^{\text{PBE}}$ (Å)	$d_{\text{av}}^{\text{PBE+SOC}}$ (Å)	$\text{ECN}^{\text{PBE}b}$	$\text{ECN}^{\text{PBE+SOC}b}$
Os	-5.43 (FCCf)	-5.32 (FCCf)	-6.56	-5.02	2	0.0	2.62	2.62	7.83 (10)	7.84 (10)
Ir	-5.35 (WHE)	-4.92 (WHE)	-5.93	-4.22	1	1.8	2.58	2.59	6.28 (7)	6.28 (7)
Pt	-5.64 (DRC)	-4.92 (DRC)	-4.47	-3.17	0	0.2	2.68	2.68	6.84 (9)	6.85 (9)
Au	-2.14 (DRC)	-2.10 (DRC)	-2.56	-2.48	1	0.7	2.80	2.79	6.52 (7)	6.53 (7)
Hg	0.00 (ICO)	0.00 (ICO)	-0.01	-0.002	0	0.0	3.59	3.58	8.39 (13)	8.41 (13)
Tl	-1.75 (PTH)	-1.72 (PTH)	-1.81	-1.11	1	0.7	3.46	3.46	8.22 (14)	8.31 (14)

^aAtomic positions for the putative global-minimum configurations (indicated in parentheses) calculated with the PBE+vdW, PBE+U, and PBE+SOC functional are provided in the Supporting Information. ^bNumber of atoms in the core region are shown in parentheses; calculated with the PBE, PBE+vdW, PBE+U, and PBE+SOC functional for selected M_{55} systems.

Figure 4, along with the results for the respective ground-state bulk structures, and the following trends were identified. (i) Except for a few systems, most of the studied metallic bulk systems are nonmagnetic, which was confirmed by our calculations (Figure 4); however, we obtained that several expected nonmagnetic systems show FM, FIM, or AFM solutions for finite-size M_{55} clusters. The FIM solution is obtained only for finite size clusters; that is, it is not obtained for the bulk systems, which is a consequence of the structural geometry of the particles due to the large number of nonequivalent atoms. (ii) In general, we obtained that m_T is larger (smaller) for compact (open) structures such as the ICO and PTH (DRC) configurations, which can be explained by the enhanced localization of the d states in compact structures.⁶⁴ (iii) For the well-known FM bulk systems, for example, Fe, Co, and Ni, we obtained larger total magnetic moments per atom for the respective TM₅₅ clusters, that is, 22.9, 20.9, and 15.9% larger, which can be attributed to the enhancement of the local magnetic moment for lower-coordinated surface atoms.

The alkali M_{55} metals are nonmagnetic as in their respective bulk phases due to the presence of only s electrons; however, m_T has nearly the same value for Sc₅₅, Y₅₅, and Lu₅₅ (i.e., about 0.65 μ_B) due to the unpaired single electron located in the d states, that is, a FM configuration. By increasing the occupation of the 3d and 4d states, $m_T \approx 0.0 \mu_B$ up to Mn₅₅ and Tc₅₅ due to the FIM or AFM interactions, for example, for Cr₅₅ and Mn₅₅. A further increase in the occupation of the 3d and 4d states yields FM solutions and high total magnetic moments, for example, Fe₅₅, Co₅₅, Ni₅₅, Ru₅₅, Rh₅₅, and Pd₅₅. Thus the present results resemble the Pauling–Slater curve,¹²⁴ which has

been explained by the occupation of the d states; the larger localization of the 3d states contributes to enhance the magnetic interactions and explains the high magnetic moments. Once the occupation of the d states is fully reached, the M_{55} are nonmagnetic. Thus although the magnitude of the total magnetic moments is smaller for the 4d M_{55} clusters, their trends are nearly the same. In contrast with the 3d and 4d systems, the 5d systems have zero or nearly zero magnetic moment for all cases, except for Lu₅₅, and hence there is a clear difference between both systems, which can be attributed to the delocalized character of the 5d states compared with the 3d and 4d states.

III.F. Role of the van der Waals Corrections. To improve the description of the M_{55} systems, we reoptimized all of the PBE configurations using the PBE+vdW functional for selected systems with weak binding energy, namely, Al₅₅, Cu₅₅, Zn₅₅, Ga₅₅, Ag₅₅, Cd₅₅, In₅₅, Au₅₅, Hg₅₅, and Tl₅₅. The most important results are summarized in Table 1. For the selected M_{55} systems, as expected, the binding energy increases for all systems due to the attractive nature of the van der Waals interactions, that is, $-\frac{C_{AB}}{R_{AB}}$, however, as noticed in Table 1, the magnitude of the enhancements is system-dependent. We found that the vdW correction reduces the relative energy with respect to the ICO structure, which implies that the vdW interactions yield a larger energy gain for compact structures such as ICO and PTH instead of open structures. This trend can be explained by the nature of the vdW correction, which is based on additive pair–pair interactions,^{75,78} and hence, it favors compact structures as in finite size particles described by

the Lennard-Jones potential;^{99,100,104} however, there are a few exceptions for this trend.

The vdW correction changes the pGMC Hg_{55} from ICO (PBE) to PTH (PBE+vdW), which is slightly less compact than ICO; that is, ECN = 7.73 NNN instead of 8.39 NNN for ICO. Furthermore, the vdW correction changes the pGMC for Ga_{55} , for example, from THL (PBE) to DRC (PBE+vdW), while In_{55} changed from an open structure, DRC (PBE), to a compact structure with high ECN, PTH (PBE+vdW). In line with that, Cd_{55} is a special case, where the DRC structure is obtained as pGMC for both PBE and PBE+vdW functionals, but there is a substantial change in the value of ECN. As the vdW correction is an attractive interaction, the bond lengths are slightly reduced, that is, <0.05%. Thus at least for the selected M_{55} systems the vdW interactions play a crucial role, and hence further studies should be performed for finite-size systems, in particular, using high-level quantum-chemistry calculations as reference data to study the performance of difference vdW corrections.^{71,75,76,78}

III.G. Role of an Enhancement in the Electron Localization. As mentioned above, to obtain a better understanding of the role of the d-state localization effects on the M_{55} properties, we performed PBE+U calculations for a selected set of systems, namely, Fe_{55} , Co_{55} , Ni_{55} , Ru_{55} , Rh_{55} , and Pd_{55} , using $U_{eff} = 2.0$ eV, and the results are summarized in Table 1. The enhancement in the electron localization is not large enough to change the pGMC for the selected systems, except for Ru_{55} , where the FCCf structure changes from PBE (eight atoms in the core region) for a FCCf structure with a larger core size (i.e., 10 atoms). For Fe_{55} the PTH pGMC is changed from a PTH motif with 12 atoms in core region to a more compact PTH pGMC, with 14 atoms in the core region. For Ni_{55} , Rh_{55} , and Pd_{55} , the structural properties show small changes, while the total magnetic moments are larger by 25, 83, and 30%, respectively. The Co_{55} is the only case where the magnetic moment does not change with an enhancement in the electron localization; however, the ICO pGMC is slightly distorted in relation to the ideal ICO obtained with plain PBE functional.

Except for Ni_{55} , we obtained a reduction of the binding energy for all selected systems, which can be explained by the increased localization of the d states that reduces the hybridization among the electronic d states and contributes to shift the occupied states down in energy, while the unoccupied states are shifted up in energy. Thus these two effects contribute to lower the binding energy. Thus the main effect of the enhancement of the electron localization is reflected in the increase in the magnetic moment, intensifies the closed-packed trend, and contributes to reduce the binding energy.

III.H. Role of the Spin–Orbit Coupling. To check the effect of SOC for M_{55} nanoclusters composed of heavy elements, we have performed additional calculations, PBE +SOC, for $M = Os, Ir, Pt, Au, Hg$, and Tl . The main results are summarized in Table 1. The same pGMC structures are obtained with and without SOC, and the relative energy with respect to the ICO structure shows small differences when PBE +SOC was included; that is, unrelaxed and relaxed systems with PBE+SOC yield about the same relative energies. The largest relative energy differences occur for Ir_{55} and Pt_{55} systems, 8.7 and 7.5% in relation to PBE+SOC calculations, respectively, while for the remaining systems the relative energy differences are <2.1%. Thus in first approximation the atomic relaxations

within PBE+SOC can be neglected, which is useful due to the high computational cost of PBE+SOC calculations. Concerning structural properties, d_{av} and ECN, we can observe very small changes between calculations with and without SOC, except for ECN of Tl_{55} systems, where the PTH structure, differently from PBE result, is not distorted for PBE-SOC results (larger ECN values). Furthermore, we obtained a reduction of the binding energy due to the addition of the SOC.

IV. SUMMARY

In this study, we performed an extensive ab initio investigation of the structural, energetic, and electronic properties of 42 metal M_{55} nanoclusters, which include 4 alkali, 4 alkaline-earth, 30 transition, and 4 post-transition metals, employing DFT within the PBE functional as implemented in VASP. Furthermore, to improve the description of the XC effects, we also considered vdW correction, SOC effects for the valence states, and the role of the electron localization of the d states using DFT-PBE+U. From our calculations, we identified a set of pGMCS and a large number of higher energy local-minimum configurations (Supporting Information), which were used to obtain an atomistic understanding of the structural, energetic, and electronic trends as a function of the atomic number.

We found a strong preference of the putative global-minimum M_{55} configurations for compact Mackay structures, where the coordination of the 13-core atoms is nearly 12, for example, 13 icosahedron structures with I_h symmetry (Na_{55} , Mg_{55} , K_{55} , Sc_{55} , Co_{55} , Ni_{55} , Cu_{55} , Rb_{55} , Y_{55} , Ag_{55} , Cs_{55} , Lu_{55} , Hg_{55}) and 3 slightly distorted icosahedron structures (Ti_{55} , Hf_{55} , Re_{55}), where the energy gain was from 0.24 to 0.40 eV compared with the ideal icosahedron structure. Furthermore, we obtained compact pGMCS that do not belong to the icosahedron-like models, for example, six polytetrahedron structures (Ca_{55} , Mn_{55} , Fe_{55} , Sr_{55} , Ba_{55} , Tl_{55}) and 10 pGMCS derived from crystalline bulk fragments, namely, 5 FCC fragments (Tc_{55} , Ru_{55} , Rh_{55} , Pd_{55} , Os_{55}) and 5 HCP fragments (Cr_{55} , Nb_{55} , Mo_{55} , Ta_{55} , W_{55}).

Therefore, we obtained 32 compact putative global-minimum structures, which are expected as the studied metals crystallize in compact structures due to the metallic bonding among the atoms, while the remaining 10 structures are based on less compact configurations such as the structural family composed of DRC structures (V_{55} , Zn_{55} , Zr_{55} , Cd_{55} , In_{55} , Pt_{55} , and Au_{55}), where the number of atoms in the core region is from 7 to 11 atoms. Furthermore, we obtained two THL (Al_{55} , Ga_{55}) and one HCP wheel-type structure (Ir_{55}).

The M_{55} binding energy shows a quasi-parabolic behavior as a function of the atomic number, which is similar to the crystals. Consequently, the same explanation employed to explain the cohesive energy behavior can be applied for M_{55} ; that is, the occupation of the bonding and antibonding states defines the main trends in the binding energy per atom. Beyond that, on average, the binding energy for M_{55} represents 79% of the cohesive energy of the respective bulk systems.

The addition of vdW correction favors compact structures, as in the case of Lennard-Jones potentials, due to the attractive nature of vdW forces that leads to an increase in the ECN values and slight change in the average bond lengths (e.g., <0.05%) for most cases. Particular systems changed their respective pGMCS; namely, Hg_{55} changed from icosahedron (PBE) to polytetrahedron (PBE+vdW), Ga_{55} changed from tetrahedral-like (PBE) to distorted reduced-core (PBE+vdW), and In_{55} changed from distorted reduced-core (PBE) to

polytetrahedron (PBE+vdW). Thus the present findings clearly indicate the importance of the role of the vdW correction for the atomic structure of nanoclusters.

Our DFT+U calculations showed that an enhancement in the electron localization of the d states changed the pGMC for particular systems, which follows similar trends obtained for the Co_{13} and Rh_{13} clusters. For example, Ru_{55} changed from a FCC fragment with 8 atoms in the core region to a structure in the same family, that is, FCC fragment, however, with 10 atoms in the region. In the same line, Fe_{55} changed from a polytetrahedron structure with 12 atoms in the core region to a polytetrahedron with 14 atoms in the core. Therefore, an enhancement in the localization of the d states contributes to increase the number of atoms in the core; that is, it increases the coordination. Furthermore, as expected, we obtained an enhancement in the total magnetic moment; for example, it was larger by 25, 83, and 30% for Ni_{55} , Rh_{55} , and Pd_{55} , respectively, while we did not obtain an enhancement in the magnetic moment for Co_{55} .

We found that the addition of the SOC for the valence states leads to tiny changes in the structural properties, namely, in the putative global-minimum structure, ECN and d_{av} . Thus, based on our calculations, we can conclude that relaxations of the atomic configurations within SOC are not required as the main effects are only on the electronic states. The same structures are obtained with and without SOC, and the relative energy differences are smaller than 2.1%, except for Ir_{55} and Pt_{55} systems, 8.7 and 7.5% in relation to PBE+SOC calculations, respectively.

Our results and findings are very useful for future studies; in particular, our reported structures can be used for a wide range of studies such as ligand effects, or core–shell formation. Therefore, we expect that the present study can be used as a database for further theoretical studies.

ASSOCIATED CONTENT

Supporting Information

The Supporting Information is available free of charge on the ACS Publications website at DOI: [10.1021/acs.jpcc.6b10404](https://doi.org/10.1021/acs.jpcc.6b10404).

Atomic structure positions of the trial atomic configurations employed in this work and partially shown in Figure 1 and atomic structure positions of all the pGMCs along with several computational details. ([PDF](#))

AUTHOR INFORMATION

Corresponding Author

*E-mail: juarez_dasilva@iqsc.usp.br. Tel: +55 16 3373 6641. Fax: +55 16 3373 9952.

ORCID

Juarez L. F. Da Silva: [0000-0003-0645-8760](https://orcid.org/0000-0003-0645-8760)

Notes

The authors declare no competing financial interest.

ACKNOWLEDGMENTS

We thank the São Paulo Research Foundation (FAPESP, 2013/21045-2, 2013/15112-9), Rio Grande do Sul Research Foundation (FAPERGS), National Council for Scientific and Technological Development (CNPq, 2013/15112-9, 301190/2015-1, 305161/2015-6), and Coordination for Improvement of Higher Level Education (CAPES) for financial support. We also thank the Laboratory of Advanced Scientific Computing

(University of São Paulo), the National Laboratory of Scientific Computing located in Petrópolis, and the Department of Information Technology – Campus São Carlos for hosting our cluster.

REFERENCES

- Zhu, Y.; Qian, H.; Jin, R. Catalysis Opportunities of Atomically Precise Gold Nanoclusters. *J. Mater. Chem.* **2011**, *21*, 6793–6799.
- Galvis, H. M. T.; Bitter, J. H.; Khare, C. B.; Ruitenbeek, M.; Dugulan, A. I.; de Jong, K. P. Supported Iron Nanoparticles as Catalysts for Sustainable Production of Lower Olefins. *Science* **2012**, *335*, 835–838.
- Wijaya, A.; Schaffer, S. B.; Pallares, I. G.; Hamad-Schifferli, K. Selective Release of Multiple DNA Oligonucleotides from Gold Nanorods. *ACS Nano* **2009**, *3*, 80–86.
- Arvizo, R. R.; Bhattacharyya, S.; Kudgus, R. A.; Giri, K.; Bhattacharya, R.; Mukherjee, P. Intrinsic Therapeutic Applications of Noble Metal Nanoparticles: Past, Present and Future. *Chem. Soc. Rev.* **2012**, *41*, 2943–2970.
- Gunawan, C.; Teoh, W. Y.; Marquis, C. P.; Lifia, J.; Amal, R. Reversible Antimicrobial Photoswitching in Nanosilver. *Small* **2009**, *5*, 341–344.
- Marambio-Jones, C.; Hoek, E. M. V. A Review of the Antibacterial Effects of Silver Nanomaterials and Potential Implications for Human Health and the Environment. *J. Nanopart. Res.* **2010**, *12*, 1531–1551.
- Kamat, P. V. Meeting the Clean Energy Demand: Nanostructure Architectures for Solar Energy Conversion. *J. Phys. Chem. C* **2007**, *111*, 2834–2860.
- Atwater, H. A.; Polman, A. Plasmonics for Improved Photovoltaic Devices. *Nat. Mater.* **2010**, *9*, 205–213.
- Schmid, G. The Relevance of Shape and Size of Au_{55} Clusters. *Chem. Soc. Rev.* **2008**, *37*, 1909–1930.
- Fernando, A.; Weerawardene, K. L. D. M.; Karimova, N. V.; Aikens, C. M. Quantum Mechanical Studies of Large Metal, Metal Oxide, and Metal Chalcogenide Nanoparticles and Clusters. *Chem. Rev.* **2015**, *115*, 6112–6216.
- Gawande, M. B.; Goswami, A.; Felpin, F.-X.; Asefa, T.; Huang, X.; Silva, R.; Zou, X.; Zboril, R.; Varma, R. S. Cu and Cu-Based Nanoparticles: Synthesis and Applications in Catalysis. *Chem. Rev.* **2016**, *116*, 3722–3811.
- Chaves, A. S.; Rondina, G. G.; Piotrowski, M. J.; Da Silva, J. L. F. Structural Formation of Binary PtCu Clusters: A Density Functional Theory Investigation. *Comput. Mater. Sci.* **2015**, *98*, 278–286.
- De Souza, D. G.; Cezar, H. M.; Rondina, G. G.; de Oliveira, M. F.; Da Silva, J. L. F. A Basin-Hopping Monte Carlo Investigation of the Structural and Energetic Properties of 55- and 561-atom Bimetallic Nanoclusters: The Examples of the ZrCu, ZrAl, and CuAl Systems. *J. Phys.: Condens. Matter* **2016**, *28*, 175302.
- Chaves, A. S.; Rondina, G. G.; Piotrowski, M. J.; Tereshchuk, P.; Da Silva, J. L. F. The Role of Charge States in the Atomic Structure of Cu_n and Pt_n ($n = 2$ –14 Atoms) Clusters: A DFT Investigation. *J. Phys. Chem. A* **2014**, *118*, 10813–10821.
- Piotrowski, M. J.; Piquini, P.; Da Silva, J. L. F. Platinum-Based Nanoalloys $\text{Pt}_n\text{TM}_{55-n}$ (TM = Co, Rh, Au): A Density Functional Theory Investigation. *J. Phys. Chem. C* **2012**, *116*, 18432–18439.
- Guedes-Sobrinho, D.; Nomiyama, R. K.; Chaves, A. S.; Piotrowski, M. J.; Da Silva, J. L. F. Structure, Electronic, and Magnetic Properties of Binary $\text{Pt}_n\text{TM}_{55-n}$ (TM = Fe, Co, Ni, Cu, Zn) Nanoclusters: A Density Functional Theory Investigation. *J. Phys. Chem. C* **2015**, *119*, 15669–15679.
- Echt, O.; Sattler, K.; Recknagel, E. Magic Numbers for Sphere Packings: Experimental Verification in Free Xenon Clusters. *Phys. Rev. Lett.* **1981**, *47*, 1121–1124.
- Knight, W. D.; Clemenger, K.; de Heer, W. A.; Saunders, W. A.; Chou, M. Y.; Cohen, M. L. Electronic Shell Structure and Abundances of Sodium Clusters. *Phys. Rev. Lett.* **1984**, *52*, 2141–2143.

- (19) Li, S. F.; Zhao, X. J.; Xu, X. S.; Gao, Y. F.; Zhang, Z. Stacking Principle and Magic Sizes of Transition Metal Nanoclusters Based on Generalized Wulff Construction. *Phys. Rev. Lett.* **2013**, *111*, 115501.
- (20) Zeng, C.; Chen, Y.; Li, G.; Jin, R. Magic Size $\text{Au}_{64}(\text{S}-\text{c-C}_6\text{H}_{11})_{32}$ Nanocluster Protected by Cyclohexanethiolate. *Chem. Mater.* **2014**, *26*, 2635–2641.
- (21) Garzón, I. L.; Michaelian, K.; Beltrán, M. R.; Posada-Amarillas, A.; Ordejón, P.; Artacho, E.; Sánchez-Portal, D.; Soler, J. M. Lowest Energy Structures of Gold Nanoclusters. *Phys. Rev. Lett.* **1998**, *81*, 1600–1603.
- (22) Wrigge, G.; Hoffmann, M. A.; Issendorff, B. V. Photoelectron Spectroscopy of Sodium Clusters: Direct Observation of the Electronic Shell Structure. *Phys. Rev. A: At., Mol., Opt. Phys.* **2002**, *65*, 063201.
- (23) Chacko, S.; Kanhere, D. G.; Blundell, S. A. First Principles Calculations of Melting Temperatures for Free Na Clusters. *Phys. Rev. B: Condens. Matter Mater. Phys.* **2005**, *71*, 155407.
- (24) Lee, M.-S.; Chacko, S.; Kanhere, D. G. First-principles Investigation of Finite-temperature Behavior in Small Sodium Clusters. *J. Chem. Phys.* **2005**, *123*, 164310.
- (25) Schooss, D.; Blom, M. N.; Parks, J. H.; Issendorff, B. v.; Haberland, H.; Kappes, M. M. The Structures of Ag_{55}^+ and Ag_{55}^- : Trapped Ion Electron Diffraction and Density Functional Theory. *Nano Lett.* **2005**, *5*, 1972–1977.
- (26) Da Silva, J. L. F.; Kim, H. G.; Piotrowski, M. J.; Prieto, M. J.; Tremiliosi-Filho, G. Reconstruction of Core and Surface Nanoparticles: The Example of Pt_{55} and Au_{55} . *Phys. Rev. B: Condens. Matter Mater. Phys.* **2010**, *82*, 205424.
- (27) Kang, J.; Kim, Y.-H. Half-Solidity of Tetrahedral-like Al_{55} Clusters. *ACS Nano* **2010**, *4*, 1092–1098.
- (28) Aguado, A.; Kostko, O. First-Principles Determination of the Structure of Na_n and Na_n^- Clusters with up to 80 Atoms. *J. Chem. Phys.* **2011**, *134*, 164304.
- (29) Wang, Z. W.; Palmer, R. E. Experimental Evidence for Fluctuating, Chiral-Type Au_{55} Clusters by Direct Atomic Imaging. *Nano Lett.* **2012**, *12*, 5510–5514.
- (30) Rapps, T.; Ahlrichs, R.; Waldt, E.; Kappes, M. M.; Schooss, D. On the Structures of 55-Atom Transition-Metal Clusters and Their Relationship to the Crystalline Bulk. *Angew. Chem., Int. Ed.* **2013**, *52*, 6102–6105.
- (31) Mackay, A. L. A Dense Non-Crystallographic Packing of Equal Spheres. *Acta Crystallogr.* **1962**, *15*, 916–918.
- (32) Barreteau, C.; Desjonquères, M. C.; Spanjaard, D. Theoretical study of the icosahedron to cuboctahedral structural transition in Rh and Pd clusters. *Eur. Phys. J. D* **2000**, *11*, 395.
- (33) Jin, R.; Zhu, Y.; Qian, H. Quantum-Sized Gold Nanoclusters: Bridging the Gap between Organometallics and Nanocrystals. *Chem. - Eur. J.* **2011**, *17*, 6584–6593.
- (34) Kittel, C. *Introduction to Solid State Physics*, 8th ed.; John Wiley & Sons, Inc.: New York, 2004.
- (35) Callister, W. D., Jr.; Rethwisch, D. G. *Materials Science and Engineering: An Introduction*; John Wiley & Sons, Inc.: New York, 2013.
- (36) Aguado, A. Structures, Relative Stabilities, and Electronic Properties of Potassium Clusters K_n ($13 \leq n \leq 80$). *Comput. Theor. Chem.* **2013**, *1021*, 135–143.
- (37) Vásquez-Pérez, J. M.; Gamboa, G. U.; Mejía-Rodríguez, D.; Alvarez-Ibarra, A.; Geudtner, G.; Calaminici, P.; Köster, A. M. Influence of Spin Multiplicity on the Melting of Na_{55}^+ . *J. Phys. Chem. Lett.* **2015**, *6*, 4646–4652.
- (38) Bergmann, T.; Martin, T. P. Observation of Electronic Shell Structure in Large Cesium Oxide Clusters. *J. Chem. Phys.* **1989**, *90*, 2848–2855.
- (39) Falconi, S.; Lundgaard, L. F.; Hejny, C.; McMahon, M. I. X-Ray Diffraction Study of Liquid Cs up to 9.8 GPa. *Phys. Rev. Lett.* **2005**, *94*, 125507.
- (40) Sen, P. Magnetism in Simple Metal and 4d Transition Metal Clusters. *J. Cluster Sci.* **2016**, *27*, 795–815.
- (41) Aguado, A.; López, J. M. Structural and Thermal Behavior of Compact Core-Shell Nanoparticles: Core Instabilities and Dynamic Contributions to Surface Thermal Stability. *Phys. Rev. B: Condens. Matter Mater. Phys.* **2005**, *72*, 205420.
- (42) Park, S.; Kim, T. J.; Chung, Y.-M.; Oh, S.-H.; Song, I. K. Direct Synthesis of Hydrogen Peroxide from Hydrogen and Oxygen Over Insoluble $\text{Pd}_{0.15}\text{M}_{2.5}\text{H}_{0.2}\text{PW}_{12}\text{O}_{40}$ ($\text{M} = \text{K}, \text{Rb}$, and Cs) Heteropolyacid Catalysts. *Res. Chem. Intermed.* **2010**, *36*, 639–646.
- (43) Bélavári, C.; András, E.; Molnár, Z.; Gawlik, D. Determination of Na, K, Rb and Cs Distribution in Human Brain Using Neutron Activation Analysis. *Microchim. Acta* **2004**, *146*, 187–191.
- (44) Guo, Y.; Bo, M.; Wang, Y.; Liu, Y.; Huang, Y.; Sun, C. Q. Atomistic Bond Relaxation, Energy Entrapment, and Electron Polarization of the Rb_n and Cs_n Clusters ($n \leq 58$). *Phys. Chem. Chem. Phys.* **2015**, *17*, 30389–30397.
- (45) Wang, G. M.; Papaconstantopoulos, D. A.; Blaisten-Barojas, E. Pressure Induced Transitions in Calcium: A Tight-binding Approach. *J. Phys. Chem. Solids* **2003**, *64*, 185–192.
- (46) Dong, X.; Wang, G. M.; Blaisten-Barojas, E. Tight-binding Model for Calcium Nanoclusters: Structural, Electronic, and Dynamical Properties. *Phys. Rev. B: Condens. Matter Mater. Phys.* **2004**, *70*, 205409.
- (47) Dai, Y.; Blaisten-Barojas, E. Energetics, Structure, and Electron Detachment Spectra of Calcium and Zinc Neutral and Anion Clusters: A Density Functional Theory Study. *J. Phys. Chem. A* **2008**, *112*, 11052–11060.
- (48) Martin, T. P. Shells of Atoms. *Phys. Rep.* **1996**, *273*, 199–241.
- (49) Wang, G. M.; Blaisten-Barojas, E.; Roitberg, A. E.; Martin, T. P. Strontium Clusters: Many-Body Potential, Energetics, and Structural Transitions. *J. Chem. Phys.* **2001**, *115*, 3640–3646.
- (50) Gong, X. G.; Zheng, Q. Q.; He, Y.-Z. Electronic Structures of Magnesium Clusters. *Phys. Lett. A* **1993**, *181*, 459–464.
- (51) Köhn, A.; Weigend, F.; Ahlrichs, R. Theoretical Study on Clusters of Magnesium. *Phys. Chem. Chem. Phys.* **2001**, *3*, 711–719.
- (52) Weigend, F.; Ahlrichs, R. Quantum Chemical Treatments of Metal Clusters. *Philos. Trans. R. Soc., A* **2010**, *368*, 1245–1263.
- (53) Rayane, D.; Melinon, P.; Cabaud, B.; Hoareau, A.; Tribollet, B.; Broyer, M. Close-packing Structure of Small Barium Clusters. *Phys. Rev. A: At., Mol., Opt. Phys.* **1989**, *39*, 6056–6059.
- (54) Boutou, V.; Allouche, A. R.; Spiegelmann, F.; Chevaleyre, J.; Frécon, M. A. Predictions of Geometrical Structures and Ionization Potentials for Small Barium Clusters Ba_n . *Eur. Phys. J. D* **1998**, *2*, 63–73.
- (55) Wang, Q.; Sun, Q.; Yu, J.-Z.; Gu, B.-L.; Kawazoe, Y.; Hashi, Y. Structures of Magic Ba Clusters and Magic Ba Suboxide Clusters. *Phys. Rev. A: At., Mol., Opt. Phys.* **2000**, *62*, 063203.
- (56) Chou, J. P.; Chen, H. Y. T.; Hsing, C. R.; Chang, C. M.; Cheng, C.; Wei, C. M. 13-Atom Metallic Clusters Studied by Density Functional Theory: Dependence on Exchange-Correlation Approximations and Pseudopotentials. *Phys. Rev. B: Condens. Matter Mater. Phys.* **2009**, *80*, 165412.
- (57) Batista, K. E. A.; Piotrowski, M. J.; Chaves, A. S.; Da Silva, J. L. F. A Theoretical Investigation of the Structural and Electronic Properties of 55-Atom Nanoclusters: The Examples of Y-Tc and Pt. *J. Chem. Phys.* **2016**, *144*, 054310.
- (58) Hohenberg, P.; Kohn, W. Inhomogeneous Electron Gas. *Phys. Rev.* **1964**, *136*, B864–B871.
- (59) Kohn, W.; Sham, L. J. Self-Consistent Equations Including Exchange and Correlation Effects. *Phys. Rev.* **1965**, *140*, A1133–A1138.
- (60) Perdew, J. P.; Chevary, J. A.; Vosko, S. H.; Jackson, K. A.; Pederson, M. R.; Singh, D. J.; Fiolhais, C. Atoms, Molecules, Solids, and Surfaces: Applications of the Generalized Gradient Approximation for Exchange and Correlation. *Phys. Rev. B: Condens. Matter Mater. Phys.* **1992**, *46*, 6671–6687.
- (61) Perdew, J. P.; Burke, K.; Ernzerhof, M. Generalized Gradient Approximation Made Simple. *Phys. Rev. Lett.* **1996**, *77*, 3865–3868.

- (62) Kresse, G.; Hafner, J. *Ab-Initio* Molecular Dynamics for Open-Shell Transition Metals. *Phys. Rev. B: Condens. Matter Mater. Phys.* **1993**, *48*, 13115–13118.
- (63) Kresse, G.; Furthmüller, J. Efficient Iterative Schemes for *Ab-Initio* Total-Energy Calculations Using a Plane-Wave Basis Set. *Phys. Rev. B: Condens. Matter Mater. Phys.* **1996**, *54*, 11169–11186.
- (64) Piotrowski, M. J.; Piquini, P.; Cândido, L.; Da Silva, J. L. F. The Role of Electron Localization in the Atomic Structure of Transition-Metal 13-atom Clusters: The Example of Co_{13} , Rh_{13} , and Hf_{13} . *Phys. Chem. Chem. Phys.* **2011**, *13*, 17242–17248.
- (65) Imada, M.; Fujimori, A.; Tokura, Y. Metal-Insulator Transitions. *Rev. Mod. Phys.* **1998**, *70*, 1039–1263.
- (66) Piotrowski, M. J.; Piquini, P.; Da Silva, J. L. F. Density Functional Theory Investigation of 3d, 4d, and 5d 13-Atom Metal Clusters. *Phys. Rev. B: Condens. Matter Mater. Phys.* **2010**, *81*, 155446.
- (67) Dudarev, S. L.; Botton, G. A.; Savrasov, S. Y.; Humphreys, C. J.; Sutton, A. P. Electron-Energy-Loss Spectra and the Structural Stability of Nickel Oxide: An LSDA+U Study. *Phys. Rev. B: Condens. Matter Mater. Phys.* **1998**, *57*, 1505–1509.
- (68) Grimme, S.; Hansen, A.; Brandenburg, J. G.; Bannwarth, C. Dispersion-Corrected Mean-Field Electronic Structure Methods. *Chem. Rev.* **2016**, *116*, 5105–5154.
- (69) Da Silva, J. L. F.; Stampfl, C.; Scheffler, M. Adsorption of Xe Atoms on Metal Surfaces: New Insights from First-Principles Calculations. *Phys. Rev. Lett.* **2003**, *90*, 066104.
- (70) Da Silva, J. L. F.; Stampfl, C.; Scheffler, M. Xe Adsorption on Metal Surfaces: First-Principles Investigations. *Phys. Rev. B: Condens. Matter Mater. Phys.* **2005**, *72*, 075424.
- (71) Grimme, S. Semiempirical GGA-Type Density Functional Constructed with a Long-range Dispersion Correction. *J. Comput. Chem.* **2006**, *27*, 1787–1799.
- (72) Lukeš, V.; Ilčin, M.; Laurinc, V.; Biskupič, S. On the Structure and Physical Origin of van der Waals Interaction in Zinc, Cadmium and Mercury Dimers. *Chem. Phys. Lett.* **2006**, *424*, 199–203.
- (73) Da Silva, J. L. F.; Stampfl, C. Nature of Xenon Adsorption on Graphite: On-top Versus Hollow Site Preference. *Phys. Rev. B: Condens. Matter Mater. Phys.* **2007**, *76*, 085301.
- (74) Da Silva, J. L. F.; Stampfl, C. Trends in Adsorption of Noble Gases He, Ne, Ar, Kr, and Xe on $\text{Pd}(111)(\sqrt{3}\times\sqrt{3})R30^\circ$: All-Electron Density-Functional Calculations. *Phys. Rev. B: Condens. Matter Mater. Phys.* **2008**, *77*, 045401.
- (75) Tkatchenko, A.; Scheffler, M. Accurate Molecular Van Der Waals Interactions from Ground-State Electron Density and Free-Atom Reference Data. *Phys. Rev. Lett.* **2009**, *102*, 073005.
- (76) Grimme, S.; Antony, J.; Ehrlich, S.; Krieg, H. A Consistent and Accurate Ab Initio Parametrization of Density Functional Dispersion Correction (DFT-D) for the 94 Elements H-Pu. *J. Chem. Phys.* **2010**, *132*, 154104.
- (77) Fernández, E. M.; Balbás, L. C. GGA Versus van der Waals Density Functional Results for Mixed Gold/Mercury Molecules and Pure Au and Hg Cluster Properties. *Phys. Chem. Chem. Phys.* **2011**, *13*, 20863.
- (78) Tkatchenko, A.; DiStasio, R. A.; Car, R.; Scheffler, M. Accurate and Efficient Method for Many-Body van der Waals Interactions. *Phys. Rev. Lett.* **2012**, *108*, 236402.
- (79) Piotrowski, M. J.; Nomiyama, R. K.; Da Silva, J. L. F. Role of van der Waals Corrections for the PtX_2 ($X = \text{O}, \text{S}, \text{Se}$) Compounds. *Phys. Rev. B: Condens. Matter Mater. Phys.* **2013**, *88*, 075421.
- (80) Bučko, T.; Lèbegue, S.; Hafner, J.; Ángyán, J. G. Tkatchenko-Scheffler van der Waals Correction Method With and Without Self-Consistent Screening Applied to Solids. *Phys. Rev. B: Condens. Matter Mater. Phys.* **2013**, *87*, 064110.
- (81) Gobre, V. V.; Tkatchenko, A. Scaling Laws for van der Waals Interactions in Nanostructured Materials. *Nat. Commun.* **2013**, *4*, 2341.
- (82) Rêgo, C. R. C.; Oliveira, L. N.; Tereshchuk, P.; Da Silva, J. L. F. Comparative Study of van der Waals Corrections to the Bulk Properties of Graphite. *J. Phys.: Condens. Matter* **2015**, *27*, 415502.
- (83) Bučko, T.; Lèbegue, S.; Hafner, J.; Ángyán, J. G. Improved Density Dependent Correction for the Description of London Dispersion Forces. *J. Chem. Theory Comput.* **2013**, *9*, 4293–4299.
- (84) Koelling, D. D.; Harmon, B. N. A Technique for Relativistic Spin-Polarised Calculations. *J. Phys. C: Solid State Phys.* **1977**, *10*, 3107–3114.
- (85) Takeda, T. The Scalar Relativistic Approximation. *Z. Phys. B: Condens. Matter Quanta* **1978**, *32*, 43–48.
- (86) Häberlen, O. D.; Chung, S.-C.; Stener, M.; Rösch, N. From clusters to bulk: A relativistic density functional investigation on a series of gold clusters Au_n , $n = 6, \dots, 147$. *J. Chem. Phys.* **1997**, *106*, 5189–5201.
- (87) Huda, M. N.; Niranjan, M. K.; Sahu, B. R.; Kleinman, L. Effect of Spin-Orbit Coupling on Small Platinum Nanoclusters. *Phys. Rev. A: At., Mol., Opt. Phys.* **2006**, *73*, 053201.
- (88) Blöchl, P. E. Projector Augmented-Wave Method. *Phys. Rev. B: Condens. Matter Mater. Phys.* **1994**, *50*, 17953–17979.
- (89) Kresse, G.; Joubert, D. From Ultrasoft Pseudopotentials to the Projector Augmented-Wave Method. *Phys. Rev. B: Condens. Matter Mater. Phys.* **1999**, *59*, 1758–1775.
- (90) Hafner, J. *Ab-Initio* Simulations of Materials Using VASP: Density-Functional Theory and Beyond. *J. Comput. Chem.* **2008**, *29*, 2044–2078.
- (91) Cordero, B.; Gómez, V.; Platero-Prats, A. E.; Revés, M.; Echeverría, J.; Cremades, E.; Barragán, F.; Alvarez, S. Covalent radii revisited. *Dalton Trans.* **2008**, 2832–2838.
- (92) Marks, L. D. Experimental Studies of Small Particle Structures. *Rep. Prog. Phys.* **1994**, *57*, 603–649.
- (93) Juhás, P.; Cherba, D. M.; Duxbury, P. M.; Punch, W. F.; Billinge, S. J. L. *Ab initio* Determination of Solid-State Nanostructure. *Nature* **2006**, *440*, 655–658.
- (94) Petkov, V.; Ohta, T.; Hou, Y.; Ren, Y. Atomic-Scale Structure of Nanocrystals by High-Energy X-ray Diffraction and Atomic Pair Distribution Function Analysis: Study of $\text{Fe}_x\text{Pd}_{100-x}$ ($x = 0, 26, 28, 48$) Nanoparticles. *J. Phys. Chem. C* **2007**, *111*, 714–720.
- (95) Yu, M.; Yankovich, A. B.; Kaczmarowski, A.; Morgan, D.; Voyles, P. M. Integrated Computational and Experimental Structure Refinement for Nanoparticles. *ACS Nano* **2016**, *10*, 4031–4038.
- (96) Erickson, J. D.; Mednikov, E. G.; Ivanov, S. A.; Dahl, L. F. Isolation and Structural Characterization of a Mackay 55-Metal-Atom Two-Shell Icosahedron of Pseudo- I_h Symmetry, $\text{Pd}_{55}\text{L}_{12}(\mu_3-\text{CO})_{20}$ ($L = \text{PR}_3$, $R = \text{Isopropyl}$): Comparative Analysis with Interior Two-Shell Icosahedral Geometries in Capped Three-Shell Pd_{145} , Pt-Centered Four-Shell $\text{Pd}-\text{Pt}$ M_{165} , and Four-Shell Au_{133} Nanoclusters. *J. Am. Chem. Soc.* **2016**, *138*, 1502–1505.
- (97) Niesse, J. A.; Mayne, H. R. Global Geometry Optimization of Atomic Clusters Using a Modified Genetic Algorithm in Space-Fixed Coordinates. *J. Chem. Phys.* **1996**, *105*, 4700–4706.
- (98) Johnston, R. L. Evolving Better Nanoparticles: Genetic Algorithms for Optimising Cluster Geometries. *Dalton Trans.* **2003**, 4193–4207.
- (99) Wales, D. J.; Doye, J. P. K. Global Optimization by Basin-Hopping and the Lowest Energy Structures of Lennard-Jones Clusters Containing up to 110 Atoms. *J. Phys. Chem. A* **1997**, *101*, 5111–5116.
- (100) Rondina, G. G.; Da Silva, J. L. F. Revised Basin-Hopping Monte Carlo Algorithm for Structure Optimization of Clusters and Nanoparticles. *J. Chem. Inf. Model.* **2013**, *53*, 2282–2298.
- (101) Rogan, J.; García, G.; Loyola, C.; Orellana, W.; Ramírez, R.; Kiwi, M. Alternative Search Strategy for Minimal Energy Nanocluster Structures: The Case of Rhodium, Palladium, and Silver. *J. Chem. Phys.* **2006**, *125*, 214708.
- (102) Tribello, G. A.; Ceriotti, M.; Parrinello, M. Using Sketch-Map Coordinates to Analyze and Bias Molecular Dynamics Simulations. *Proc. Natl. Acad. Sci. U. S. A.* **2012**, *109*, 5196–5201.
- (103) Ceriotti, M.; Tribello, G. A.; Parrinello, M. Demonstrating the Transferability and the Descriptive Power of Sketch-Map. *J. Chem. Theory Comput.* **2013**, *9*, 1521–1532.
- (104) Lennard-Jones, J. E.; Devonshire, A. F. Critical Phenomena in Gases. I. *Proc. R. Soc. London, Ser. A* **1937**, *163*, 53–70.

- (105) Sutton, A. P.; Chen, J. Long-Range Finnis-Sinclair Potentials. *Philos. Mag. Lett.* **1990**, *61*, 139–146.
- (106) Daw, M. S.; Baskes, M. I. Semiempirical, Quantum Mechanical Calculation of Hydrogen Embrittlement in Metals. *Phys. Rev. Lett.* **1983**, *50*, 1285–1288.
- (107) Daw, M. S.; Foiles, S. M.; Baskes, M. I. The Embedded-Atom Method: A Review of Theory and Applications. *Mater. Sci. Rep.* **1993**, *9*, 251–310.
- (108) Grigoryan, V. G.; Alamanova, D.; Springborg, M. Structure and Energetics of Cu_N Clusters with (2 ≤ N ≤ 150): An Embedded-Atom-Method Study. *Phys. Rev. B: Condens. Matter Mater. Phys.* **2006**, *73*, 115415.
- (109) Hennes, M.; Buchwald, J.; Ross, U.; Lotnyk, A.; Mayr, S. G. Equilibrium Segregation Patterns and Alloying in Cu/Ni Nanoparticles: Experiments Versus Modeling. *Phys. Rev. B: Condens. Matter Mater. Phys.* **2015**, *91*, 245401.
- (110) Baletto, F.; Ferrando, R. Structural Properties of Nanoclusters: Energetic, Thermodynamic, and Kinetic Effects. *Rev. Mod. Phys.* **2005**, *77*, 371–423.
- (111) Ferrando, R.; Jellinek, J.; Johnston, R. L. Nanoalloys: From Theory to Applications of Alloy Clusters and Nanoparticles. *Chem. Rev.* **2008**, *108*, 845–910.
- (112) Ferrando, R. Symmetry Breaking and Morphological Instabilities in Core-Shell Metallic Nanoparticles. *J. Phys.: Condens. Matter* **2015**, *27*, 013003.
- (113) Cox, A. J.; Louderback, J. G.; Bloomfield, L. A. Experimental Observation of Magnetism in Rhodium Clusters. *Phys. Rev. Lett.* **1993**, *71*, 923–926.
- (114) Cox, A. J.; Louderback, J. G.; Apsel, S. E.; Bloomfield, L. A. Magnetism in 4d-Transition Metal Clusters. *Phys. Rev. B: Condens. Matter Mater. Phys.* **1994**, *49*, 12295–12298.
- (115) Gehrke, R.; Reuter, K. Assessing the Efficiency of First-Principles Basin-Hopping Sampling. *Phys. Rev. B: Condens. Matter Mater. Phys.* **2009**, *79*, 085412.
- (116) Doye, J. P. K.; Wales, D. J. Polytetrahedral Clusters. *Phys. Rev. Lett.* **2001**, *86*, 5719–5722.
- (117) Alonso, J. A. Electronic and Atomic Structure, and Magnetism of Transition-Metal Clusters. *Chem. Rev.* **2000**, *100*, 637–678.
- (118) Wang, S.-Y.; Yu, J.-Z.; Mizuseki, H.; Yan, J.-A.; Kawazoe, Y.; Wang, C.-Y. First-Principles Study of the Electronic Structures of Icosahedral Ti_n (*n* = 13, 19, 43, 55) Clusters. *J. Chem. Phys.* **2004**, *120*, 8463–8468.
- (119) Lee, M.-S.; Kanhere, D. G. Effects of Geometric and Electronic Structure on the Finite Temperature Behavior of Na₅₈, Na₅₇, and Na₅₅ Cluster. *Phys. Rev. B: Condens. Matter Mater. Phys.* **2007**, *75*, 125427.
- (120) Hoppe, R. The Coordination Number – An “Inorganic Chameleon. *Angew. Chem., Int. Ed. Engl.* **1970**, *9*, 25–34.
- (121) Hoppe, R. Effective Coordination Numbers (ECoN) and Mean Active Fictive Ionic Radii (MEFIR). *Z. Kristallogr.* **1979**, *150*, 23–52.
- (122) Da Silva, J. L. F. Effective Coordination Concept Applied for Phase Change (GeTe)_m(Sb₂Te₃)_n Compounds. *J. Appl. Phys.* **2011**, *109*, 023502.
- (123) Holbrow, C. H.; Lloyd, J. N.; Amato, J. C.; Galvez, E.; Parks, M. E. *Hard-Sphere Atoms*; Springer: New York, 2010; pp 109–149.
- (124) Harrison, W. A. *Electronic Structure and the Properties of Solids: The Physics of the Chemical Bond*; Dover Publications, Inc.: New York, 1980.